

# Prospective motion correction and automatic segmentation of penetrating arteries in phase contrast MRI at 7 T

Julia Moore<sup>1</sup> | Jordan Jimenez<sup>1</sup> | Weili Lin<sup>1,2</sup> | William Powers<sup>3</sup> | Xiaopeng Zong<sup>1,2</sup> 

<sup>1</sup>Biomedical Research Imaging Center, University of North Carolina at Chapel Hill, Chapel Hill, North Carolina, USA

<sup>2</sup>Department of Radiology, University of North Carolina at Chapel Hill, Chapel Hill, North Carolina, USA

<sup>3</sup>Department of Neurology, University of North Carolina at Chapel Hill, Chapel Hill, North Carolina, USA

## Correspondence

Xiaopeng Zong, Department of Radiology and Biomedical Research Imaging Center, University of North Carolina at Chapel Hill, CB#7515 Chapel Hill, NC 27599, USA.

Email: [zongxp@gmail.com](mailto:zongxp@gmail.com)

## Funding information

National Institutes of Health, Grant/Award Number: 5R21NS095027-02; National Center for Advancing Translational Sciences (NCATS), National Institutes of Health, Grant/Award Number: UL1TR002489

**Purpose:** To develop a prospective motion correction (MC) method for phase contrast (PC) MRI of penetrating arteries (PAs) in centrum semiovale at 7 T and to evaluate its performance using automatic PA segmentation.

**Methods:** Head motion was monitored and corrected during the scan based on fat navigator images. Two convolutional neural networks (CNN) were developed to automatically segment PAs and exclude surface vessels. Real-life scans with MC and without MC (NoMC) were performed to evaluate the MC performance. Motion score was calculated from the ranges of translational and rotational motion parameters. MC versus NoMC pairs with similar motion scores during MC and NoMC scans were compared. Data corrupted by motion were reacquired to further improve PA visualization.

**Results:** PA counts ( $N_{PA}$ ) and PC and magnitude contrasts (MgC) relative to neighboring tissue were significantly correlated with motion score and were higher in MC than NoMC images at motion scores above 0.5–0.8 mm. Data reacquisition further increased PC but had no significant effect on  $N_{PA}$  and MgC. CNNs had higher sensitivity and Dice similarity coefficient for detecting PAs than a threshold-based method.

**Conclusions:** Prospective MC can improve the count and contrast of segmented PAs in the presence of severe motion. CNN-based PA segmentation has improved performance in delineating PAs than the threshold-based method.

## KEYWORDS

convolutional neural network, image segmentation, penetrating arteries, phase contrast MRI, prospective motion correction

## 1 | INTRODUCTION

Cerebral small vessel disease (SVD) is a condition postulated to have multiple different etiologies. It may result from a cascade of events, starting with endothelial dysfunction in the penetrating arteries (PAs).<sup>1</sup> Other possible causes include the thickening of the arterial media due to lipohyalinosis or obstruction of the origins of PAs

by parent artery intimal plaques, which lead to brain ischemia resulting in deep small infarcts and leakage of fluid causing edema and later gliosis in white matter (WM) tracts.<sup>2</sup> Additionally, inflammation might also be involved in the development of PA leakage and endothelial dysfunction, although the causal relationships are yet to be established.<sup>3</sup> Cumulatively, SVD might

lead to substantial cognitive,<sup>4–6</sup> psychiatric,<sup>7</sup> and physical impairment.<sup>8,9</sup>

Phase contrast (PC) MRI is a common method for imaging arteries and can visualize a large number of PAs (27–91) in centrum semiovale at 7 T.<sup>10,11</sup> One major concern that arises during imaging is the susceptibility to motion which reduces PA visibility and might introduce artificial group differences due to different motion tendencies between the participants. As the PC MRI only covers a single slice, prospective motion correction (MC) is needed to ensure consistent imaging location in the presence of head motion. In this study, we will evaluate the improvements of PA visualization by prospective MC based on motion parameters derived from whole-brain fat navigator (FatNav) images.<sup>12</sup>

Accurate segmentation of PA is a key step in objective evaluation of improved PA visualization by MC and in future studies delineating the roles of PAs in SVD. Automatic PA segmentation can increase objectivity and avoid tedious manual segmentation in large image sets, although it may still carry biases. Existing automatic segmentation methods relied on applying thresholds on the phase difference (PD) and magnitude images to delineate PAs which only controls for false positive rates, but might suffer from a high false negative rate due to the low contrast to noise ratio of some PAs in the images.<sup>10,11</sup> Here, we evaluate the performance of a two-dimensional multichannel multiscale encoder decoder network (M2EDN) for segmenting the PAs, which was adopted from a three-dimensional (3D) M2EDN originally developed for perivascular spaces (PVS) segmentation.<sup>13</sup> Furthermore, since some arteries on cortical surface mimic PA, a WM mask can be applied to remove such false PAs and further improve segmentation accuracy. To this end, we also developed a 3D U-NET to segment the WM masks on 3D T<sub>2</sub>-weighted (T2w) images that were acquired during the same imaging sessions.<sup>14</sup>

## 2 | METHODS

### 2.1 | Subjects

This study was approved by the Institutional Review Board of the University of North Carolina at Chapel Hill. Written informed consents were obtained from all subjects before the scans. Two separate experiments were performed: Experiment 1 (Exp 1) acquired images used for training the convolutional neural network (CNN) parameters and Experiment 2 (Exp 2) was carried out to evaluate the performance of MC. 39 healthy volunteers (aged 21–55 years, 28 females) were included in Exp 1 and 22 patients with diabetes and 17 healthy controls (aged 37–70 years, 22

females) were included in Exp 2. As this study focuses only on evaluation of segmentation and MC methods, the comparison of PA features between patients and healthy controls will not presented here.

### 2.2 | Data acquisition

All images were acquired on a 7T MRI scanner (Siemens Healthineer). In Exp 1, a 32-channel receiver and 8-channel transmitter head coil (Nova Medical) was used. No radio frequency magnetic field (B<sub>1</sub>) shimming was performed. In Exp 2, the images were acquired using a Nova 32-channel receiver and single-channel volume transmitter coil. The subjects were asked to keep their heads still during all scans.

A 3D variable flip angle turbo spin echo (TSE) sequence (TR = 3 or 3.4 s; TE = 326 ms; TA = 8:03 min) was used to acquire T2w images with voxel size =  $0.41 \times 0.4 \times 0.4 \text{ mm}^3$  for WM segmentation.<sup>15,16</sup> A FatNav image<sup>12</sup> was acquired within each TR to monitor head motion. In Exp 1, the FatNav images (voxel size =  $2.2 \times 2.2 \times 2.2 \text{ mm}^3$ , TE/TR/TA = 1.5 ms/3.1 ms/0.89 s, flip angle = 7°) were not utilized to correct motion in the present study, although they had been utilized to perform retrospective MC in a separate study.<sup>17</sup> In Exp 2, the FatNav images (voxel size =  $3 \times 3 \times 3 \text{ mm}^3$ , TE/TR/TA = 1.31 ms/3 ms/0.47 s, flip angle = 7°) were used to measure motion parameters relative to the first FatNav image and perform prospective MC.

Then, a single slice PC MRI scan (TR = 30 ms; TE = 15.7 ms; TA = 3:13 min, NA = 10, no cardiac trigger) was performed to image PAs in centrum semiovale. The slice was positioned 15 mm above the corpus callosum and parallel to the anterior – posterior commissure line. No FatNav was acquired for the PC MRI scans in Exp 1. In Exp 2, the FatNav and PC MRI data were acquired alternately as shown in the sequence diagram in Figure 1. The FatNav had the same spatial resolution, field of view, and TE as in the TSE sequence but different TR (30 ms) and flip angle (14°). The FatNav image TR was 4.68 s. Motion parameters were received 2.1 s after the completion of each FatNav image acquisition due to reconstruction and registration times. The addition of the FatNav module into the PC-MRI sequence did not increase TR in Exp 2 as compared to Exp 1, since the duration of the FatNav module was only 3.5 ms. After acquiring and reconstructing each FatNav image, motion parameters were estimated using vendor software on the scanner (MOCO functor) and the PC-MRI slice position and readout, phase encoding, and slice normal directions were adjusted accordingly. As the slice was prescribed based on the TSE images, to correct for potential motion between the TSE and PC MRI scans,

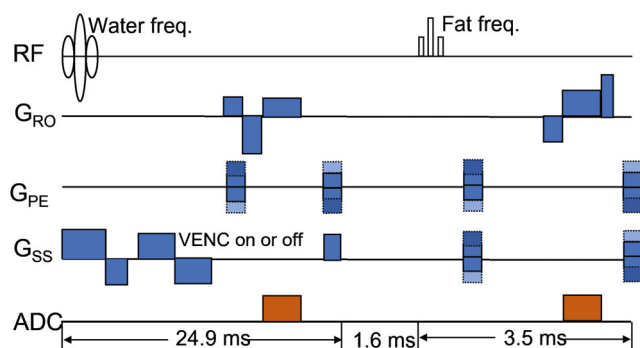


**FIGURE 1** Pulse sequence of the phase contrast-MRI sequence interleaved with fat navigator (FatNav) acquisition. The widths of the different modules do not scale with their durations. The total durations of the phase contrast and FatNav modules and the separation between them are provided at the bottom of the figure.

the FatNavs in PC MRI were registered to the first FatNav from the TSE-MRI scan.

Because of the relative long time for FatNav acquisition and reconstruction (6.78 s), motion occurred during this period cannot be corrected. Therefore, reacquiring k-space data during periods with large motion may further improve image quality. For this purpose, k space data were divided by the times when the motion parameter feedbacks were received into blocks. Define  $T_{\max}$  and  $R_{\max}$  as the maximum translational and rotational motions that occurred during acquisition of the data block and associated FatNavs. The data block was reacquired if  $T_{\max} > 0.1$  mm or  $R_{\max} > 0.1^\circ$ . The details of  $T_{\max}$  and  $R_{\max}$  calculation can be found in Section 1 of Supporting Information Appendix S1. After data reacquisition completed, the same criterion was used to determine whether the required data needed to be reacquired once more. The scan stopped until no further reacquisition was needed or the total reacquisition time exceeded the original scan time.

Three types of PC MRI scans were performed: (1) MC on but reacquisition off, (2) both MC and reacquisition on, (3) both MC and reacquisition off while FatNavs was still acquired (denoted as NoMC). The number of subjects undergoing each scan type is shown in Supporting Information Figure S1. In total, 39, 75, and 20 scans were acquired for Types 1, 2, and 3, respectively. Furthermore, to study whether the insertion of the FatNav module into the sequence would impact the quality of PC MRI images, the scan type 1 and the conventional PC MRI scan without the FatNav module were acquired in an additional subject with the subject keeping his head still in both scans.

At the beginning of each sequence that contained FatNavs, a navigator image that included fully sampled data at the k-space center was acquired for image reconstruction. The undersampled k-space for FatNav was filled line

by line and top-down through k-space. The parameters for all the sequences are provided in Supporting Information Table S1.

## 2.3 | Segmentation

### 2.3.1 | U-NET and M2EDN for automatic PA segmentation

The U-NET for segmentation of TSE images output five probability images corresponding to the background, thalamus, basal ganglia (BG), WM, and midbrain, respectively. Each voxel was assigned to the tissue type with the highest probability among the 5 images. The PD images and the magnitude images (referring to the ones with flow encoding gradient off throughout the paper) from the PC MRI were input to a modified M2EDN network for segmenting PAs. The network output a probability map and pixels with probability above 0.8 within the WM masks were classified as PA.

The networks were trained using masks manually drawn on the TSE and PC-MRI images from Exp 1. All images were used for training the final models to be used for segmenting images in Exp 2. In addition, to evaluate segmentation performances, we divided the images into 10 groups wherein each subject was assigned to only one of the 10 groups. Nine groups were used for training and the remaining one for testing the segmentation performance, and training was repeated for each of the 10 possible combinations. Using the group that was left out for testing, we analyzed segmentation performances of our networks using sensitivity (SEN), positive predictive value (PPV), and Dice similarity coefficient (DSC) as:

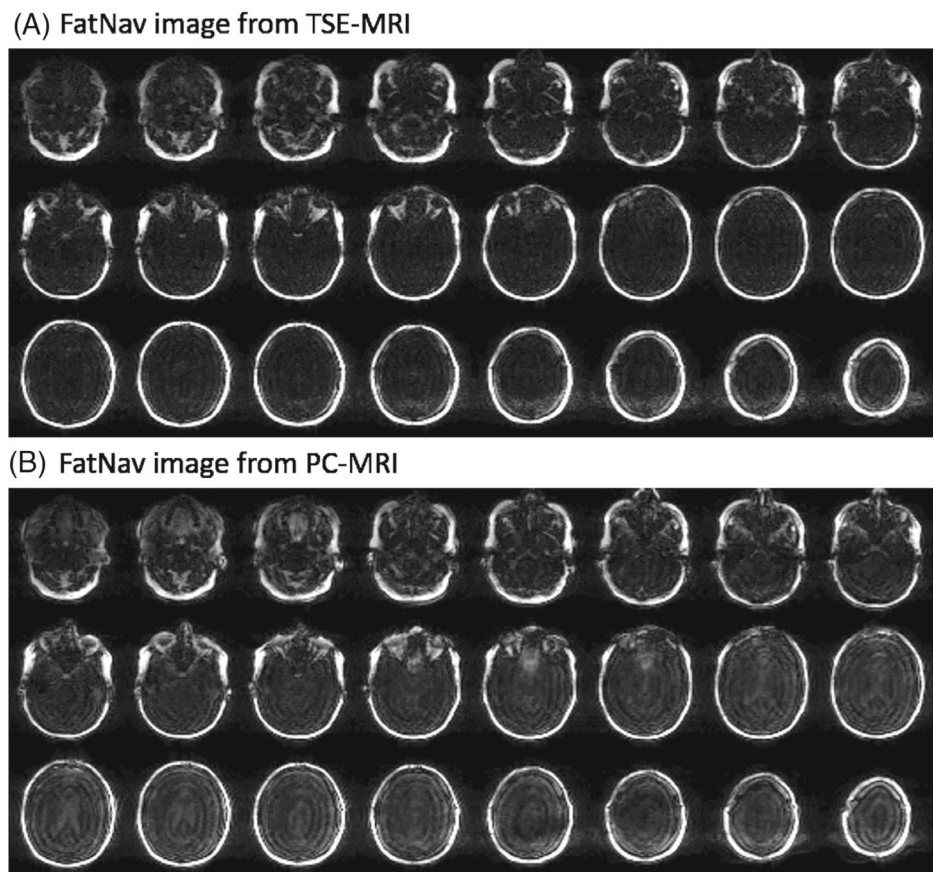
$$\text{PPV} = \text{TP} / (\text{TP} + \text{FP})$$

$$\text{SEN} = \text{TP} / (\text{TP} + \text{FN})$$

$$\text{DSC} = 2\text{TP} / (2\text{TP} + \text{FP} + \text{FN}),$$

where TP, FP, and FN stand for the number of true positive, false positive, and false negative voxels, respectively, using the manually drawn masks as ground truth. Additionally, since the true size of PAs were less than 1 voxel in the PC MRI images and the main goal of the segmentation algorithm was to simply detect visible PAs, but not to delineate their spatial extent, the three parameters were also calculated using TP, FP, FN for true positive, false positive, and false negative spatially connected clusters. A predicted cluster is considered to be a true cluster if it spatially overlaps with a cluster in the ground truth mask. The WM masks were applied to remove false PA voxels outside

**FIGURE 2** Representative fat navigator images acquired in the (A) TSE and (B) phase contrast (PC)-MRI sequences.



the WM before calculating both the voxel and cluster level parameters.

Further details of the ground truth, CNN architectures, and model training can be found in Sections 2–4 of Supporting Information Appendix S1.

### 2.3.2 | WM mask for PC MRI

The WM masks are needed both for normalizing the image intensities of the input images to M2EDN and for removing false PA voxels. To generate the WM masks, we first obtained the 3D WM masks by segmenting the TSE images with U-NET and then resampled the masks at the pixel positions of the PC MRI images. Then, the resampled WM masks were manually adjusted to account for possible head movement between the T2w and PC MRI scans (Exp 1) or for a slight mismatch between prescribed and measured slice positions even after MC. The mismatch was caused by subtle differences between the FatNav images acquired during the TSE and PC MRI sequences, as can be seen in Figure 2. As a result of the subtle differences, there existed systematic errors (nonzero biases) in estimated motion parameters. The above procedure generated the WM masks for 50 of the 61 PC MRI images in Exp 1, as spatially aligned 3D WM masks were unavailable in the

remaining subjects. For those remaining subjects, the WM masks were manually drawn.

### 2.3.3 | Conventional WM and PA segmentation

For comparison, we also obtained PA and WM masks using a threshold-based method<sup>10</sup> and the FAST segmentation tool in FSL,<sup>18</sup> respectively. Further details can be found in Section 5 of Supporting Information Appendix S1.

## 2.4 | Data analysis

### 2.4.1 | Image reconstruction

Details of FatNav image reconstruction has been described before,<sup>17</sup> where we applied the GRAPPA reconstruction algorithm.<sup>19</sup> The TSE images were reconstructed by the vendor provided software on the scanner.

PC MRI images were reconstructed offline to a voxel size of  $0.1563 \times 0.1563 \text{ mm}^2$  by zero padding in k-space before inverse Fourier transform. Images from repetitions 2–10 were averaged. The first repetition was discarded because there was inherent slice position inconsistency



between k-space data acquired before and after receiving the first feedback during the first repetition. The inconsistency can be caused by head motion between the TSE and PC-MRI scans and/or the above-mentioned systematic error in motion parameters. Then, coil-combined PD and magnitude images were obtained as described in Reference 10.

To study whether replacing data affected by motion can further improve image quality, we reconstructed images after replacing a data block in the original acquisition by a reacquired block at the same k-space locations if  $T_{\max} + R_{\max}$  of the original block ( $T_{\max, \text{orig}} + R_{\max, \text{orig}}$ ) is greater than that of the reacquired block ( $T_{\max, \text{racq}}$  and  $R_{\max, \text{racq}}$ ). Additionally, to mitigate cases where the above condition was met simply due to measurement errors in  $T_{\max}$  and  $R_{\max}$ , but not due to actual motion in the original acquisition, we also reconstructed images by enforcing the following two additional criteria for data replacement: (1)  $T_{\max, \text{orig}}$  or  $R_{\max, \text{orig}}$  are above certain thresholds, and (2)  $T_{\max, \text{racq}}$  and  $R_{\max, \text{racq}}$  are below the same thresholds. Five different thresholds were used from (0.1 mm, 0.1 deg) to (0.5 mm, 0.5 deg) in step of (0.1 mm, 0.1 deg).

## 2.4.2 | Motion parameters

To investigate whether the differences in PA parameters between MC and NoMC scans depended on the motion severity, rotational ( $M_R$ ) and translational ( $M_T$ ) motion ranges were calculated for all scans.  $M_R$  ( $M_T$ ) was defined as the root mean square of the differences of the maximum and minimum values of the three rigid-body rotational (translational) parameters of all FatNav images acquired during repetitions 2–10. Note that the motion parameters were estimated assuming the axes for rotation passed through the center of the field of view. A motion score was defined as:  $\text{score} = M_T + 57.3 \text{ mm} \times M_R$ , where  $M_T$  and  $M_R$  are in units of mm and radians, respectively. The motion score is similar to that defined in Reference 20 and corresponds to adding to  $M_T$  a shift caused by rotation  $M_R$  of a point on the surface of a sphere with a radius of 57.3 mm. For simplicity, the radius of 57.3 mm is chosen instead of the 64 mm in Reference 20 such that the score is simply equal to the sum of  $M_T$  and  $M_R$  when they are in units of mm and degrees, respectively.

## 2.4.3 | PA parameters

The PC MRI images in Exp 2 were segmented using the trained M2EDN described in Section 2.3.1. The number of PAs ( $N_{\text{PA}}$ ) was calculated as the number of spatially connected clusters in the final masks after excluding false

PA voxels outside the WM masks. Furthermore, we calculate phase and magnitude contrasts (denoted as PC and MgC) between PA clusters and neighboring WM voxels and averaged them over all PA clusters that match between a “MC vs NoMC” (MC-NoMC) pair or between a pair of images with versus without data replacement (denoted as DR pair) from Type 2 scans. Details of PC and MgC calculations are provided in Section 6 of Supporting Information Appendix S1.

The MC-NoMC pairs were formed by pairing the NoMC (Type 3) scan with each of the MC scans (Types 1 and 2) in the same subject, with only images without data replacement used for Type 2 scans. The image pairs were visually inspected and those showing clear slice coverage mismatch (likely due to motion during or before the NoMC scans) between the two images were excluded. As a result, images from five subjects were excluded, resulting in 44 pairs for comparison. On the other hand, there were 75 DR pairs for comparing the effects of data replacement.

The MC-NoMC pairs were divided into three groups based on the difference in motion scores within each pair. The pairs with motion score difference between MC and NoMC  $< -0.4$  mm, between  $-0.4$  mm and  $0.4$  mm, and  $> 0.4$  mm were defined as having less, similar, and more motion during MC scan, respectively. The threshold of  $0.4$  mm is roughly twice the sum of root mean squares of residual standard deviations of the rotational and translational parameters estimated in our previous study.<sup>17</sup> Among the 44 pairs, there were 11, 28, 5 pairs that had less, similar, and more motion during the MC scans, respectively. The mean and range of the motion scores for each group are given in Table S2. Only the 28 pairs with similar motion will be presented in the main text, while comparison of the other pairs will be described in Section 7 in Supporting Information Appendix S1.

## 2.4.4 | Statistical analysis

Wilcoxon's signed rank tests were performed to compare the PPV, SEN, and DSC values of the conventional and CNN-based segmentation methods. For PA segmentation, the threshold scale of the conventional method for comparison was chosen as the one that had the largest DSC. To evaluate the effects of MC and data reacquisition, Wilcoxon's signed rank tests were also performed to compare the PA parameters with MC versus NoMC and with versus without data replacements. Furthermore, we calculated the Spearman's correlation coefficients between the PA parameter differences in MC-NoMC pairs and the motion scores (means over the MC vs. NoMC pairs), and between the PA parameter differences in DR pairs and the percentage of data replaced.

For all statistical tests,  $p$  values less than 0.05 are considered significant after Bonferroni correction for multiple comparison (i.e. comparing multiple parameters).

### 3 | RESULTS

Table 1 (Rows 1–4) provides SEN, PPV, and DSC values for the four ROIs segmented by U-NET. SEN values are highest for thalamus (0.82) and lowest for midbrain (0.68). PPV values across all four ROIs range between 0.8 and 0.89 and DSC values range from 0.74 to 0.85, indicating a high degree of similarity between the U-NET and GT segmentations of the four ROIs. For comparison, the SEN, PPV, and DSC of the FAST WM masks are shown in Row 5. The PPV and DSC of FAST are significantly lower than those of U-NET ( $p = 0.0020$ ), while SEN is not significantly different ( $p = 0.375$ ). Figure 3 shows representative T2w slices that intersect the four brain regions and the overlaying ROIs generated by the trained U-NET model.

Figure 4A shows representative PD and magnitude images with overlaying PA masks generated by the M2EDN. Two false PAs were detected in a sulcus of the brain, as denoted by the arrows, which were removed by applying the WM mask as shown in Figure 4B. Table 1 (Rows 6 and 7) gives SEN, PPV, and DSC values of the M2EDN masks evaluated at the voxel and cluster levels. The cluster level values are higher than the corresponding voxel level ones with the DSC value reaching a high value of 0.83. Figure 5 compares the SEN, PPV, and DSC of the M2EDN and threshold-based masks, where the results are plotted at different thresholds above which potential PA voxels were defined. The SEN, PPV, and DSC of the threshold-based masks reach maximum at threshold scales of 3, 8, and 7, respectively. At threshold scale of

7, all the three parameters are significantly lower than those of the M2EDN masks at both voxel and cluster levels (corrected  $p \leq 0.012$ , Wilcoxon's signed rank test).

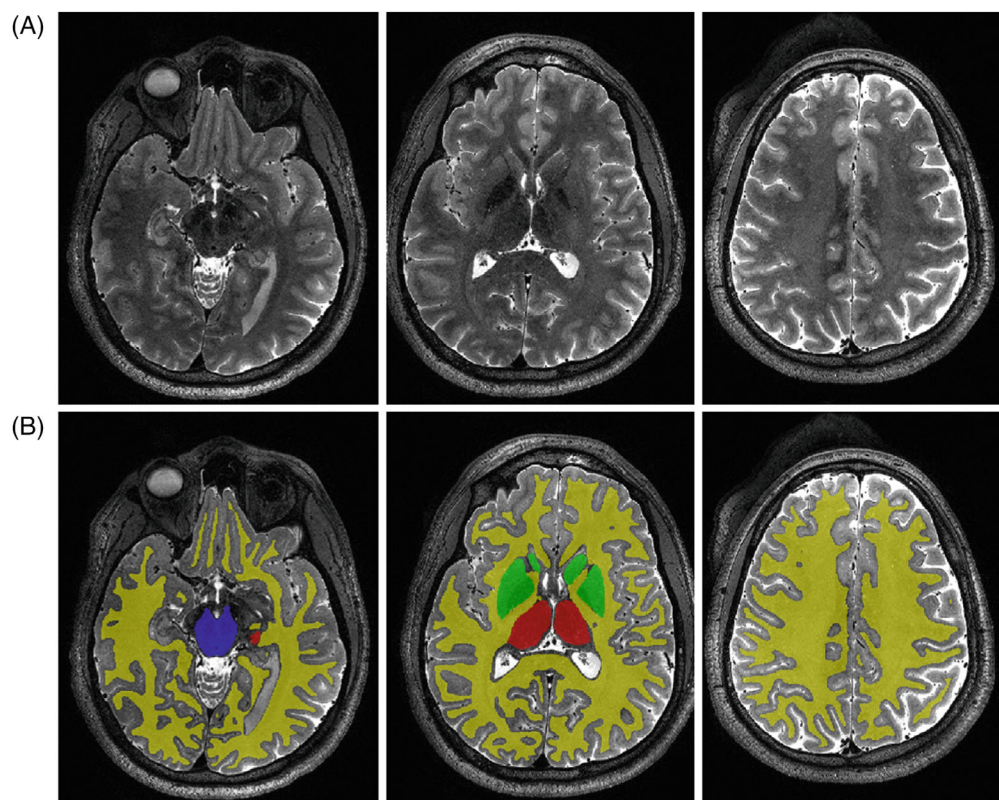
Figure 6A,B shows PD and magnitude images acquired with prospective MC and with the conventional PC MRI without the FatNav module, respectively, and without intentional head motion in both scans. The motion range as measured by FatNav were only  $M_T = 0.27$  mm and  $M_R = 0.15^\circ$  in the scan with prospective MC, while the amount of motion was unknown for the scan without FatNav. The artifact levels were similar both in the brain and the background between (A) and (B), demonstrating that the FatNav module did not negatively affect image quality.

Figure 7 shows PC-MRI images from a representative MC-NoMC pair with similar motion, where PAs appear to have higher contrast on the images with MC. The head motion parameters were similar between the MC and NoMC scans, where  $M_T = 0.79$  mm (MC) versus 0.59 mm (NoMC) and  $M_R = 0.53^\circ$  (MC) versus  $0.54^\circ$  (NoMC). Motion traces for the two scans can be found in Figure S2. More PAs were segmented by M2EDN in the images with MC, as shown in the last row of Figure 7.

Figure 8A–C shows the strong positive correlations of the differences of  $N_{PA}$ , PC, and MgC between images in MC-NoMC pairs with mean motion scores (corrected  $p < 0.023$ ; Spearman's correlation). Interestingly, the  $y$ -intercept of the best-fitted lines are negative and the motion scores below which the fitted lines for  $N_{PA}$ , PC, and MgC are negative are 0.81, 0.68, and 0.48 mm, respectively. Table 2 (Columns 1–3) give the  $N_{PA}$ , PC, and MgC averaged over the MC-NoMC pairs. The images with MC had significantly higher MgC (corrected  $p = 0.007$ ), but no difference in  $N_{PA}$  and PC compared to the NoMC images. In total, 46%, 48%, and 78% pairs had higher  $N_{PA}$ , PC, and MgC in images with MC, respectively.

**TABLE 1** Sensitivity (SEN), predictive value (PPV), and dice similarity coefficient (DSC) of thalamus, basal ganglia (BG), midbrain, and white matter (WM) masks obtained using U-NET segmentation of T2w images (rows 1–4), of the WM masks from FAST (row 5), and of penetrating artery masks (rows 6 and 7) obtained using the multichannel multiscale encoder decoder network (M2EDN) segmentation of phase contrast (PC)-MRI images in Exp 1. The results (except for row 5) are averages across the 10 combinations of the training and testing data groups. The numbers in parentheses are standard deviations.

		SEN	PPV	DSC
U-NET	Thalamus	0.77 (0.11)	0.91 (0.07)	0.83 (0.07)
	BG	0.79 (0.08)	0.80 (0.16)	0.78 (0.09)
	Midbrain	0.59 (0.24)	0.90 (0.05)	0.68 (0.22)
	WM	0.74 (0.09)	0.88 (0.07)	0.79 (0.03)
FAST	WM	0.77 (0.09)	0.61 (0.12)	0.68 (0.10)
M2EDN	Voxel - level	0.56 (0.12)	0.82 (0.07)	0.66 (0.08)
	Cluster - level	0.80 (0.10)	0.87 (0.08)	0.83 (0.06)



**FIGURE 3** (A) Representative T2w images in a single subject. (B) Overlaid U-NET tissue segmentation masks. The yellow, green, red, and blue regions are white matter, basal ganglia, thalamus, and midbrain, respectively.

Figure 8D–F shows the scatter plots of  $N_{PA}$ , PC, and MgC changes after data replacement versus the percentage of replaced data, when no motion score threshold for data replacement was imposed. No significant correlation was observed for  $N_{PA}$  and MgC ( $p \geq 0.41$ ), while a significant positive correlation was observed for PC (corrected  $p = 0.014$ ). Table 2 (Columns 4–6) gives the  $N_{PA}$ , PC, and MgC averaged over the DR pairs. The images with data replacement had significantly higher PC (corrected  $p = 0.0012$ ), but no difference in  $N_{PA}$  and MgC compared to the images without replacement. Similar results were obtained when the threshold of  $(0.1 \text{ mm}, 0.1^\circ)$  was applied on  $T_{max}$  and  $R_{max}$ . When larger thresholds were adopted, no significant change in PA parameters by data replacement was observed. The changes in PA parameters for all data replacement criteria and the Spearman's correlation coefficients with percentage of replaced data can be found in Table S3.

## 4 | DISCUSSION

In this study, we developed CNN-based automatic segmentation methods for both WM and PAs based on 3D U-NET and M2EDN, respectively. The CNNs increased the SEN, PPV, and DSC of PA delineation compared to the conventional threshold-based method. We then used these automatic segmentations to evaluate the performance of

prospective MC for improving PA visualization in 2D PC MRI. Compared to the NoMC scans with similar motion scores, MC improved the visualization of PA in a motion score dependent manner, as evidenced by positive  $N_{PA}$ , PC, and MgC changes at large motion scores. Reacquiring data affected by head motion could further increase PC, but had no significant effect on  $N_{PA}$  or MgC.

Although CNN-based tissue segmentation of 7 T healthy brain MRI images has been reported before,<sup>21,22</sup> our study is the first to evaluate the performance of such an approach for WM segmentation based on T2w images. CEREBRUM-7T employed a deep encoder/decoder network with three layers and achieved high DSC of 0.9 and 0.86 in WM and BG.<sup>21</sup> However,  $T_1$ -weighted images which have higher gray-WM contrast were employed. In our study, we acquired the T2w images instead because they have higher contrast to noise ratio for imaging PVS.<sup>15</sup> Although PVS results are not included in this paper, it will be important to study PVS and PAs together as they are both integral parts of the glymphatic system.<sup>23</sup> Another study segmented gray matter in 7T ex vivo T2w images with  $0.3 \times 0.3 \times 0.3 \text{ mm}^3$  resolution and achieved DSC of 78.5% to 98.5%. However, the WM was not segmented.<sup>22</sup>

Our M2EDN outperformed the threshold-based method for segmenting PAs for all three metrics except for the voxel level SEN at threshold scales of 3–6. However, there were large numbers of false positive voxels at such threshold scales, resulting in low PPVs. The low PPVs



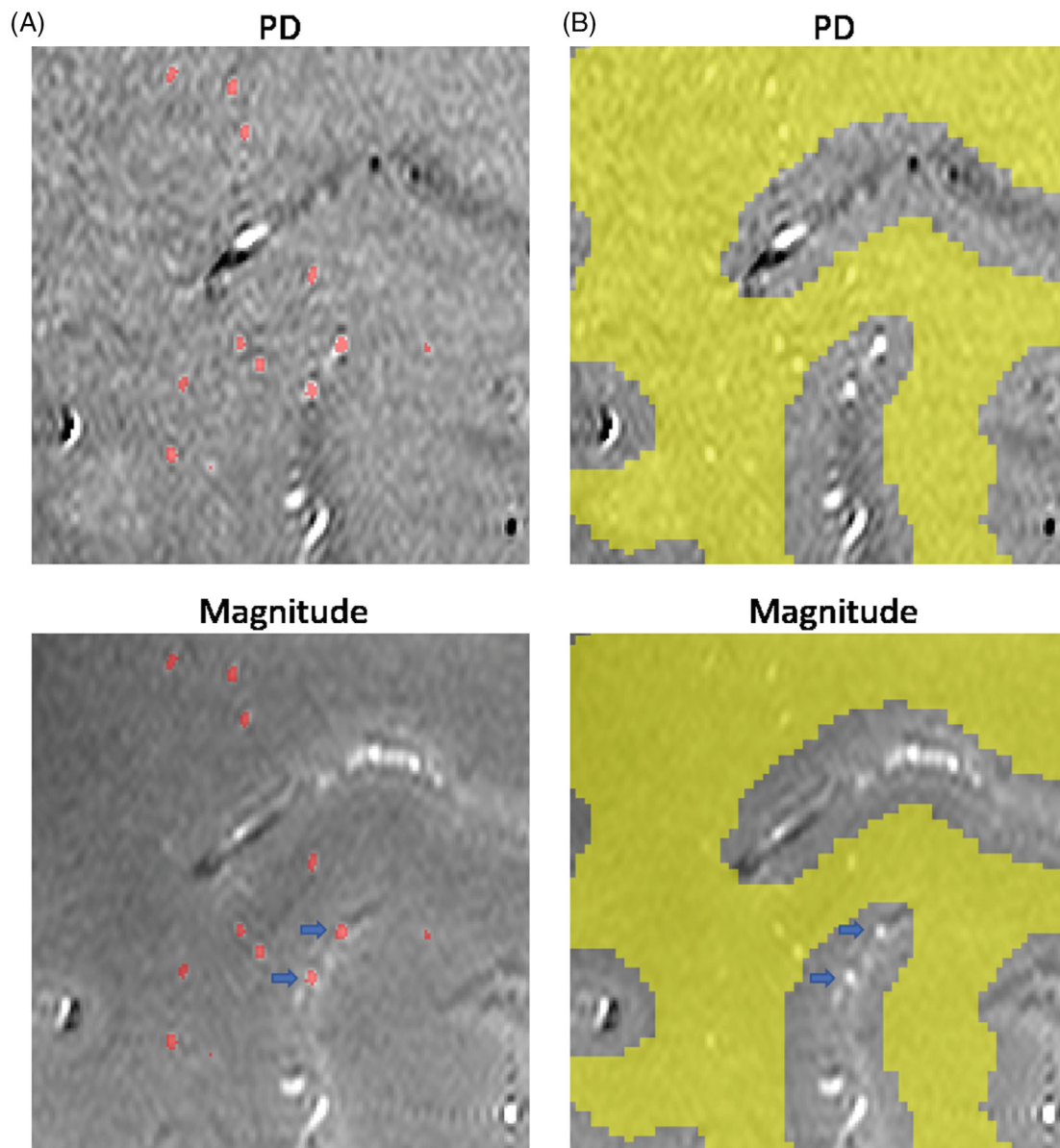


**FIGURE 4** (A) Phase difference and magnitude images of a representative subject overlaid with penetrating artery masks segmented by multichannel multiscale encoder decoder network. (B) Resampled WM mask generated from the U-NET shown in yellow. The arrows denote two false positive clusters on the cortical surface.

even at the highest threshold scale studied suggest that without manual correction, the threshold-based method cannot effectively control for the false positive rate, possibly due to imaging artifacts and intrinsic limitations of the median filter for removing the background signal.

Our main motivation for adopting navigator-based MC is that it does not require any external hardware, marker attachment, or calibration. Although navigator-based MC has been incorporated into various MRI sequences,<sup>20,24–30</sup> it has never been applied to PC MRI. In previous applications, a complete dataset of navigator echo or image were acquired in a single time block. This is impractical for PC MRI due to its short repetition time. Therefore, the k-space

data for navigator and main images were acquired in an interleaved fashion. A second distinction from previous studies is that the fat signal was used for navigators which allows one to optimize the flip angle to maximize the signal to noise ratio in the navigator data without saturation effects on the main images.<sup>27</sup>

Interleaving the PC-MRI and FatNav modules may introduce image artifacts due to possible interferences between them. In our PC-MRI sequence, we applied a constant gradient along the slice-selection direction after readout to spoil the residual transverse magnetization. The additional gradients from the FatNav module might negate the effect of the spoiler gradients. To prevent this from



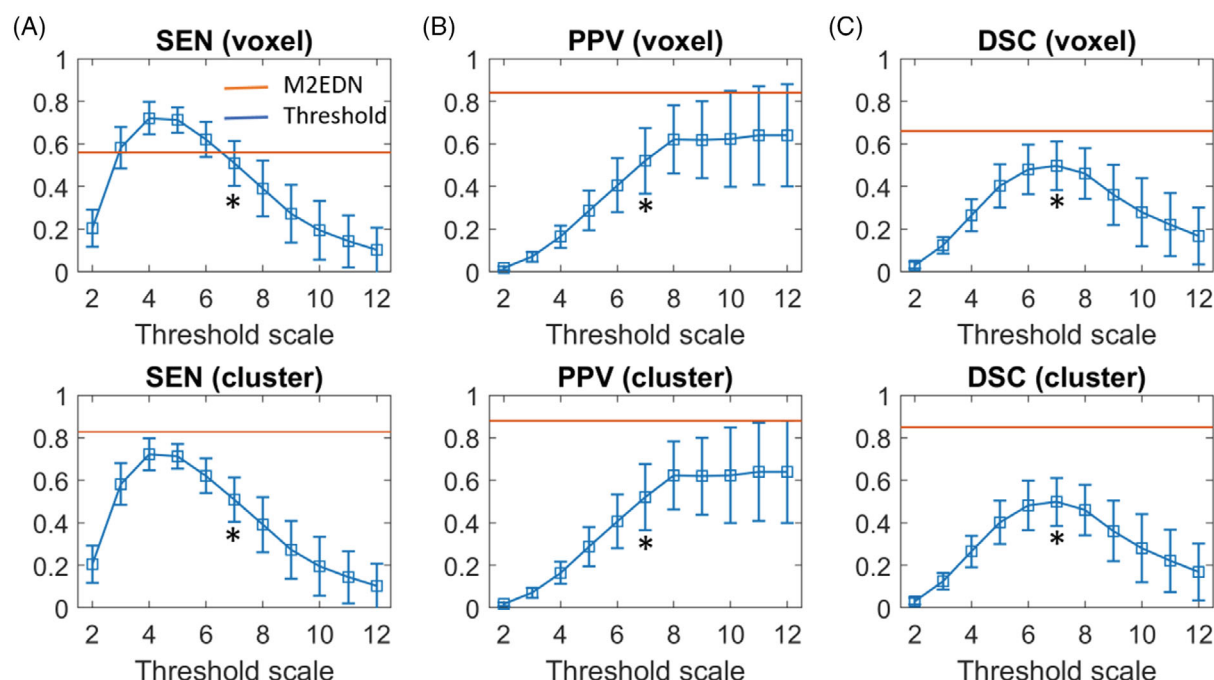
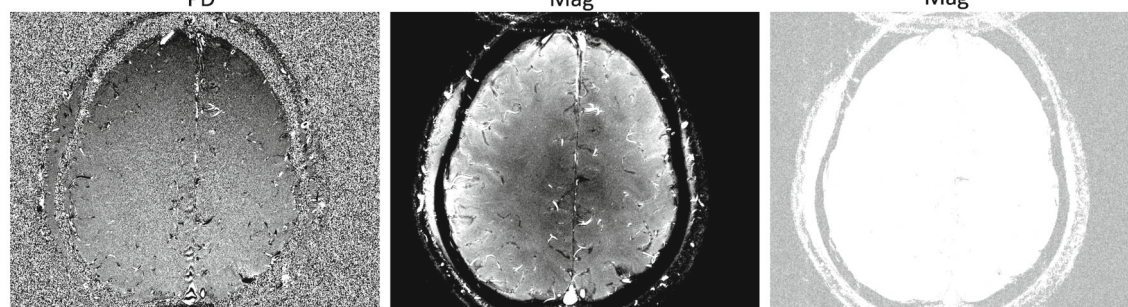


**FIGURE 5** (A) Sensitivity, (B) positive predictive value, and (C) dice similarity coefficient of penetrating artery masks obtained using the multichannel multiscale encoder decoder network (M2EDN) (red line) and threshold-based method at different threshold scaling factors (blue curve). The top and bottom rows are calculated at the voxel and cluster levels, respectively. The asterisks denote significant difference between M2EDN and threshold-based masks when threshold scale = 7.

(A) With FatNav module and MC on PD



(B) No FatNav module PD

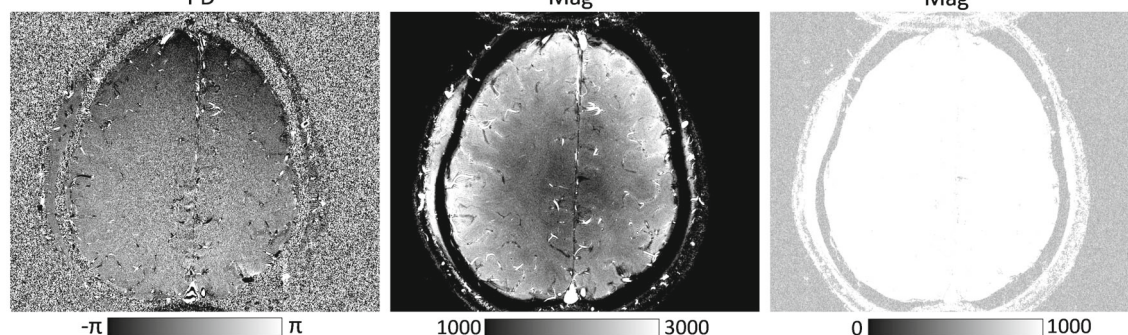


**FIGURE 6** Comparison of phase difference (PD) and magnitude (Mag) images from phase contrast MRI acquired (A) with and (B) without the fat navigator module. Motion correction (MC) was turned on in (A). The intensity window in the right column is chosen to show possible ghosting artifacts in the background.

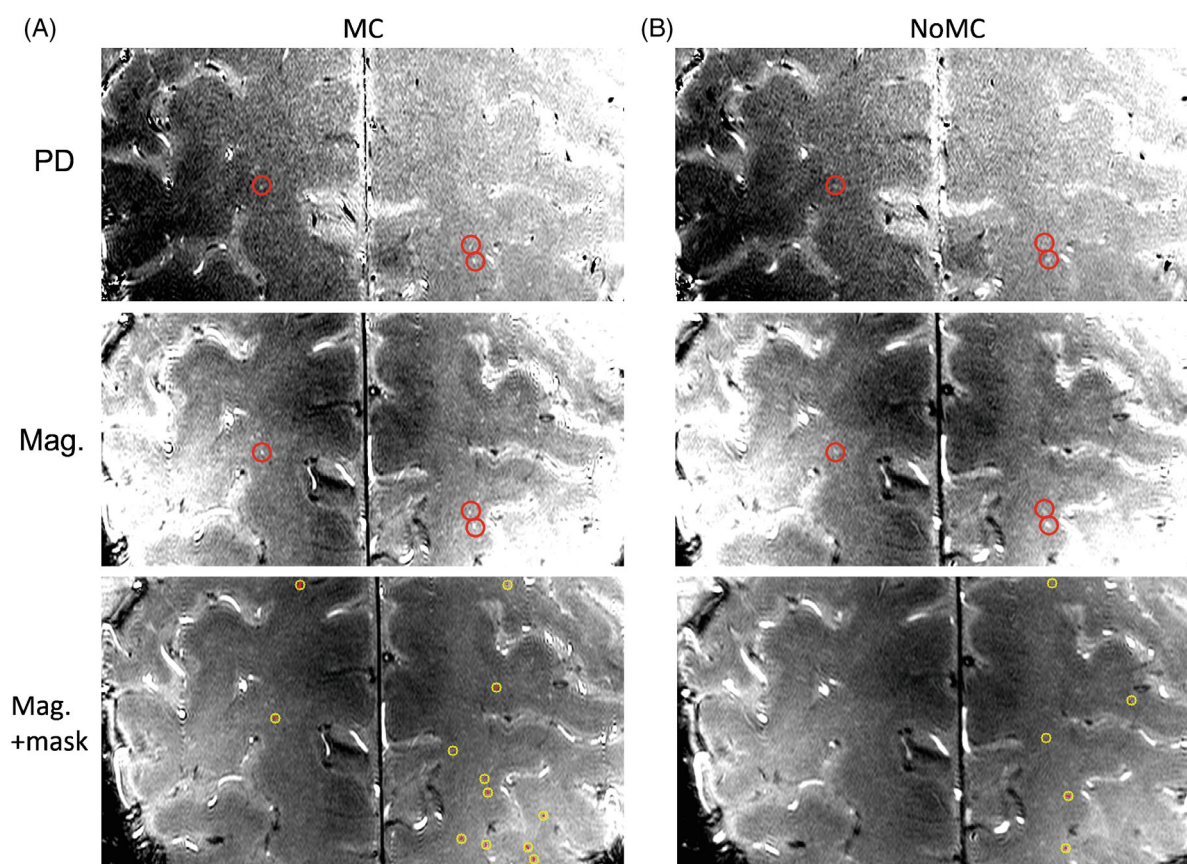


**FIGURE 7** Comparison of phase contrast (PC)-MRI images with (A) MC and (B) NoMC in a MC-NoMC pair with similar motion. The red circles enclose penetrating arteries (PAs) that show higher contrast in (A) than in (B). The PA masks generated by multichannel multiscale encoder decoder network are shown in the last row. To guide the eye, yellow circles are placed around the segmented PAs.

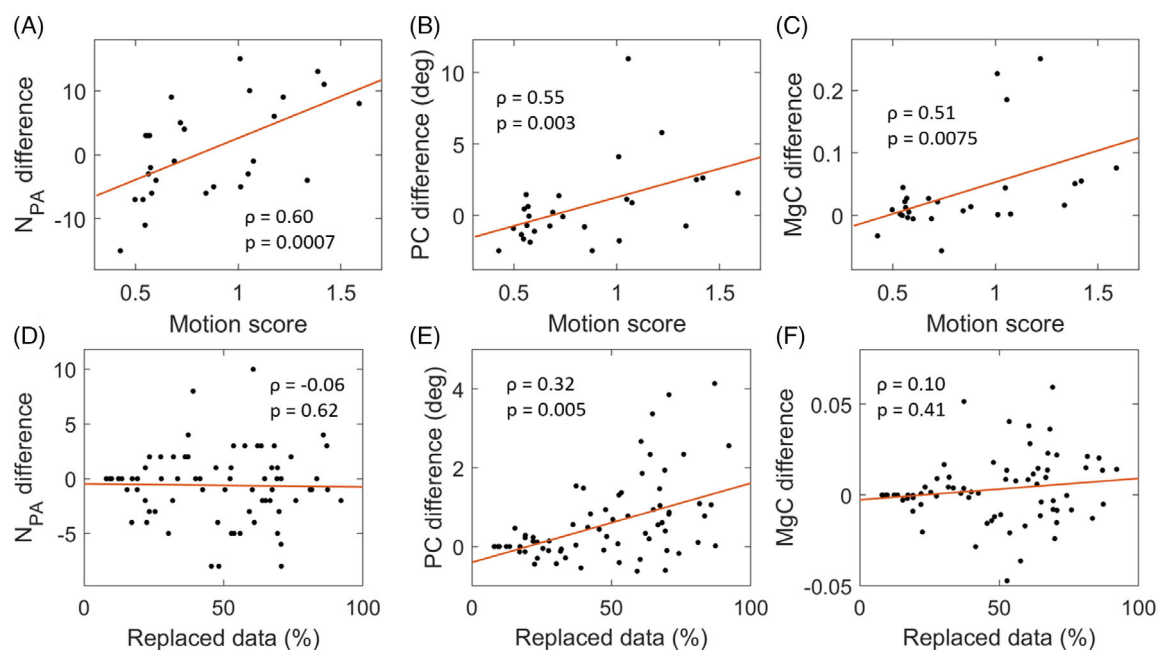


**FIGURE 8** (A–C) Scatter plots of (A)  $N_{PA}$ , (B) phase contrast (PC), and (C) magnitude contrasts (MgC) differences between motion correction (MC) and NoMC images versus the mean motion score in the MC-NoMC pairs. (D–F) Scatter plots of (D)  $N_{PA}$ , (E) PC, and (F) MgC differences between images with and without data replacement versus the percent of replaced data in the DR pairs. The red lines are least square fits. The Spearman's correlation coefficients and associated p values (without Bonferroni correction) are also given.



**TABLE 2** Penetrating artery (PA) parameters averaged over the images in the motion correction (MC)-NoMC pairs (columns 1 and 2) with similar motion and data replacement (DR) pairs (columns 4 and 5). The numbers in the parentheses are standard deviations. Columns 3 and 6 give the p values (number of pairs) of Wilcoxon's signed tests comparing the parameters between the two groups to their left. No motion score threshold was applied in reconstructing images in the DR pairs. Note that the number of MC-NoMC pairs for phase contrast (PC) and magnitude contrasts (MgC) is one less than for  $N_{PA}$  because there was no matched PA cluster in one of the pairs.

	MC vs. NoMC			Data replacement		
	MC	No MC	p value (n)	Replacement	No replacement	p value (n)
$N_{PA}$	29.3 (9.0)	28.6 (13.5)	0.68 (28)	31.9 (14.8)	32.5 (14.8)	0.088 (75)
PC (deg)	18.9 (3.6)	18.3 (2.6)	0.65 (27)	18.9 (2.6)	18.5 (2.5)	0.0003 (75)
MgC	0.36 (0.07)	0.33 (0.04)	0.0022 (27)	0.35 (0.06)	0.34 (0.07)	0.56 (75)

occurring, we set the zeroth moments of the gradients in the FatNav module to be constant and no extra artifact was observed in the PC-MRI image as shown in Figure 6. On the other hand, the FatNav module consists of a balanced steady-state free precession sequence. The addition of the PC-MRI module violates the balanced gradient condition. In addition, residual water signal that was not completed spoiled might be detected during FatNav readout. As a result, the FatNav images from PC-MRI showed increased artifact level within the brain compared to those in the TSE sequence (see Figure 2B). The artifacts may have contributed to the systematic bias in motion parameters, since they were absent in the reference FatNav image from the TSE scans.

We found that MC increased  $N_{PA}$ , PC, and MgC only when the motion score is above 0.5–0.8 mm and the increases were larger at higher motion score. This finding is consistent with the expectation that MC would not improve image quality when there is no or little motion because of the limited accuracy of motion parameter estimates. Instead, MC might be detrimental to image quality in such cases since the errors in motion parameter estimates can introduce additional noise into the images, consistent with the observed negative changes in the PA parameters. In addition, the limited temporal resolution of FatNav and the bias in the estimated motion parameters can negatively affect the motion parameter accuracy and thus image quality.

We found that data reacquisition increased PC but had no significant effect on  $N_{PA}$  and MgC. The reason for the differential effects on PC and MgC is unknown. However, the lack of significant improvement on  $N_{PA}$  suggests that reacquisition did not improve the visualization of PAs, which might be attributed to the following reasons. First, in contrast to the correction of deliberate large motions in previous studies,<sup>20,26</sup> our study focused on real-life scanning conditions in which subjects were not asked to make deliberate large head movements, but to keep as still as possible. After applying prospective MC, decent image qualities were obtained in most cases even

without data reacquisition, leaving less room for further improvement with data reacquisition. Second, due to the relative long TR to acquire the complete k-space data for each FatNav image, fast head motion may not be detected. Third, although approximately 10%–90% data blocks were replaced by reacquired data using our criteria, some of them may not truly represent data with more motion due to the intrinsic measurement errors in  $M_T$  and  $M_R$  and the small scores of the true motion. To reduce the fraction of data replaced simply because of measurement errors in  $M_T$  and  $M_R$  but no actual motion, we applied stricter criteria for data replacement as specified in Section 2.4.1. However, significant improvements were still not observed for  $N_{PA}$  and MgC.

There are several proposed causes of SVD. One in particular is the occlusion of PAs which can result in a lacunar infarct downstream of the occlusion. On PC MRI images, occluded arteries without blood flow will not appear on the scan. Fewer identified arteries in our segmentations could be an indicator of potential diseased PAs. Longitudinal studies could assess how factors such as cholesterol level, blood pressure, or blood glucose levels affect the blood flow through PAs. Furthermore, observing whether blood flow improves or worsens with therapeutic interventions could be useful for developing effective prevention and treatment strategies for SVD.

Our study has several limitations. First, due to different sequence parameters for FatNav between T2w and PC MRI scans, there existed a systematic error in the motion parameters. In the future, more accurate image registration algorithm should be developed. Second, due to the relative long TR and reconstruction time of FatNav, only gradual motion can be corrected. Faster motion detection approaches such as those based on free induction decay signal should be explored in future development,<sup>31,32</sup> which may enable further improvement in image quality by reacquiring data corrupted by accidental rapid head motion. However, physiological brain motion, such as those due to respiration and cardiac pulsation, still cannot be corrected, which will cause residual



blurring of PAs and reduction of  $N_{PA}$ . Furthermore, sliding window or pseudo-random compressed sensing acquisition/reconstruction of FatNav data should also be explored for increasing the temporal resolution of motion parameter measurement.<sup>33,34</sup> Third, we only characterized the motion using motion score while the type of motion and the k-space location at which motion took place were ignored which were also important factors of image quality. The motion score thresholds of 0.5–0.8 mm might change in subjects with different motion characteristics.

## 5 | CONCLUSIONS

We have developed a prospective MC method for PC MRI which improved the contrast and count of segmented PAs in centrum semiovale at 7 T when motion score is above 0.5–0.8 mm. Furthermore, we have improved the overall performance of PA segmentation using CNN-based approaches. The improved PA imaging and segmentation methods may help illuminate the mechanisms of pathophysiological changes of PAs in SVD.


## ACKNOWLEDGMENTS

The project described was partly supported by United States National Institutes of Health through grant 5R21NS095027-02 and the National Center for Advancing Translational Sciences (NCATS), National Institutes of Health, through Grant Award Number UL1TR002489.

## DATA AVAILABILITY STATEMENT

Images and the code for CNN-based segmentation are available in Mendeley Data (<https://data.mendeley.com/datasets/sx72xyfvbv/1>).

## ORCID

Xiaopeng Zong  <https://orcid.org/0000-0003-4235-6948>

## REFERENCES

- Wardlaw JM. Small vessel disease: mechanisms and clinical implications. *Lancet*. 2019;18:684-696.
- Caplan LR. Lacunar infarction and small vessel disease: pathology and pathophysiology. *J Stroke*. 2015.
- Low A, Mak E, Rowe JB, Markus HS. Inflammation and cerebral small vessel disease: a systematic review. *Ageing Res Rev*. 2019;53:100916.
- Van Der Flier WM, van Straaten EC, Barkhof F, et al. Small vessel disease and general cognitive function in nondisabled elderly: the LADIS study. *Stroke*. 2005;36:2116-2120.
- Kalaria RN, Erkinjuntti T. Small vessel disease and subcortical vascular dementia. *J Clin Neurol*. 2006;2:1-11.
- Kisler K, Nelson AR, Montagne A, Zlokovic BV. Cerebral blood flow regulation and neurovascular dysfunction in Alzheimer disease. *Nat Rev Neurosci*. 2017;18:419-434.
- Herrmann LL, Le Masurier M, Ebmeier KP. White matter hyperintensities in late life depression: a systematic review. *J Neurol Neurosurg Psychiatry*. 2008;79:619-624.
- De Laat KF, Tuladhar AM, Van Norden AG, Norris DG, Zwiers MP, de Leeuw FE. Loss of white matter integrity is associated with gait disorders in cerebral small vessel disease. *Brain*. 2011;134:73-83.
- Mestre H, Kostrikov S, Mehta RI, Nedergaard M. Perivascular spaces, glymphatic dysfunction, and small vessel disease. *Clin Sci*. 2017;131:2257-2274.
- Zong X, Lin W. Quantitative phase contrast MRI of penetrating arteries in centrum semiovale at 7T. *NeuroImage*. 2019;195:463-474.
- Geurts L, Biessels GJ, Luijten P, Zwanenburg J. Better and faster velocity pulsatility assessment in cerebral white matter perforating arteries with 7T quantitative flow MRI through improved slice profile, acquisition scheme, and postprocessing. *Magn Reson Med*. 2018;79:1473-1482.
- Gallichan D, Marques JP, Gruetter R. Retrospective correction of involuntary microscopic head movement using highly accelerated fat image navigators (3D FatNavs) at 7T. *Magn Reson Med*. 2016;75:1030-1039.
- Lian C, Zhang J, Liu M, et al. Multi-channel multi-scale fully convolutional network for 3D perivascular spaces segmentation in 7T MR images. *Med Image Anal*. 2018;46:106-117.
- Ronneberger O, Fischer P, Brox T. U-Net: convolutional networks for biomedical image segmentation. *MICCAI*. 2015;9351:234-241.
- Zong X, Park SH, Shen D, Lin W. Visualization of perivascular spaces in the human brain at 7T: sequence optimization and morphology characterization. *Neuroimage*. 2016;125:895-902.
- Busse RF, Hariharan H, Vu A, Brittain JH. Fast spin echo sequences with very long echo trains: design of variable refocusing flip angle schedules and generation of clinical T2 contrast. *Magn Reson Med*. 2006;55:1030-1037.
- Zong X, Nanavati S, Hung SC, Li T, Lin W. Effects of motion and retrospective motion correction on the visualization and quantification of perivascular spaces in ultrahigh resolution T2-weighted images at 7T. *Magn Reson Med*. 2021;18:1944-1955.
- Zhang Y, Brady M, Smith S. Segmentation of brain MR images through a hidden Markov random field model and the expectation-maximization algorithm. *IEEE Trans Med Imaging*. 2001;20:45-57.
- Griswold MA, Jakob PM, Heidemann RM, et al. Generalized autocalibrating partially parallel acquisitions (GRAPPA). *Magn Reson Med*. 2002;47:1202-1210.
- Tisdall MD, Hess AT, Reuter M, Meintjes EM, Fischl B, van der Kouwe AJ. Volumetric navigators for prospective motion correction and selective reacquisition in neuroanatomical MRI. *Magn Reson Med*. 2012;68:389-399.
- Svanera M, Benini S, Bontempi D, Muckli L. CEREBRUM-7T: fast and fully volumetric brain segmentation of 7 tesla MR volumes. *Hum Brain Mapp*. 2021;42:5563-5580.
- Khandelwal P. Gray matter segmentation in ultra high resolution 7 tesla ex vivo T2w MRI of human brain hemispheres. arXiv, 2021. 2110.07711.
- Iliff JJ, Wang M, Zeppenfeld DM, et al. Cerebral arterial pulsation drives paravascular CSF-interstitial fluid exchange in the murine brain. *J Neurosci*. 2013;33:18190-18199.

24. Lee CC, Grimm RC, Manduca A, et al. A prospective approach to correct for inter-image head rotation in fMRI. *Magn Reson Med*. 1998;39:234-243.
25. White N, Roddey C, Shankaranarayanan A, et al. PROMO: Real-time prospective motion correction in MRI using image-based tracking. *Magn Reson Med*. 2010;63:91-105.
26. Frost R, Hess AT, Okell TW, et al. Prospective motion correction and selective reacquisition using volumetric navigators for vessel-encoded arterial spin labeling dynamic angiography. *Magn Reson Med*. 2016;76:1420-1430.
27. Hoinkiss DC, Porter DA. Prospective motion correction in 2D multishot MRI using EPI navigators and multislice-to-volume image registration. *Magn Reson Med*. 2017;78:2127-2135.
28. Mattern H, Sciarra A, Lüsebrink F, Acosta-Cabronero J, Speck O. Prospective motion correction improves high-resolution quantitative susceptibility mapping at 7T. *Magn Reson Med*. 2019;81:1605-1619.
29. Mattern H, Sciarra A, Godenschweger F, et al. Prospective motion correction enables highest resolution time-of-flight angiography at 7T. *Magn Reson Med*. 2018;80:248-258.
30. Simegn GL, Van der Kouwe AJ, Robertson FC, Meintjes EM, Alhamud A. Real-time simultaneous shim and motion measurement and correction in glycoCEST MRI using double volumetric navigators (DvNavs). *Magn Reson Med*. 2018;81:2600-2613.
31. Kober T, Marques JP, Gruetter R, Krueger G. Head motion detection using FID navigators. *Magn Reson Med*. 2011;66:135-143.
32. Wallace TE, Afacan O, Waszak M, Kober T, Warfield SK. Head motion measurement and correction using FID navigators. *Magn Reson Med*. 2019;81:258-274.
33. Xu Z, Ye H, Lyu M, et al. Rigid motion correction for magnetic resonance fingerprinting with sliding-window reconstruction and image registration. *Magn Reson Imaging*. 2019;57:303-312.
34. Gamper U, Boesiger P, Kozerke S. Compressed sensing in dynamic MRI. *Magn Reson Med*. 2008;59:365-373.

## SUPPORTING INFORMATION

Additional supporting information may be found in the online version of the article at the publisher's website.

### Appendix S1: Supporting Information

**Figure S1:** The flow diagram of the types of scans performed on different subjects. The first number next to each text box gives the number of repetitions of each scan type, while the number in the parenthesis is the total number of subjects undergoing such scans.

**Figure S2:** Motion parameter traces during the (A) NoMC and (B) MC scans in Figure 7, showing similar degrees of motion during the MC and NoMC scans. Different colors represent different motion directions or rotation axes.

**Figure S3:** The temporal relationship between the PC-MRI data blocks and FatNav acquisitions. The curly brackets denote the time periods during which motion will affect the given motion parameters or  $D_i$ .

**Figure S4:** The architecture of the 3D U-NET for brain tissue segmentation. The numbers above the rectangles specify the dimensionality of the output space, while the numbers above the pink arrows specify the dropout rate of the Dropout layer.

**Table S1:** MRI parameters for the TSE, PC, and FatNav sequences. In the PC sequence,  $VENC = 4$  cm/s and a one-sided flow encoding were employed, thereby the flow encoding gradient was turned on and off alternately in different TRs.

**Table S2:** Mean (standard deviation) and range of motion scores in MC-NoMC pairs with similar, less, and more motion during MC. The third column gives p values (number of samples) from Wilcoxon's signed rank tests comparing the motion scores.

**Table S3:** Mean changes in PA parameters after data replacements. The different columns correspond to applying different threshold requirements for  $T_{max}$  (units: mm) and  $R_{max}$  (units: deg) as described in Section 2.4.1. The numbers in the parentheses in the first and remaining rows are the total number of images and the standard deviations, respectively. The third number in each entry of rows 3–5 is the Spearman's correlation coefficient between the change and the fraction of replaced data. An asterisk denotes significant difference from 0 or significant correlation after Bonferroni correction.

**Table S4:** PA parameters averaged over the images in the MC-NoMC pairs with less (columns 1 and 2) or more (columns 4 and 5) motion during the MC scan. The numbers in the parenthesis are standard deviations. Columns 3 and 6 give the p values (number of pairs) of Wilcoxon's signed tests comparing the parameters between the two groups to their left. Note that the number of MC-NoMC pairs for PC and MgC might be less than for  $N_{PA}$  because there were no matched PA clusters in some of the pairs.

**How to cite this article:** Moore J, Jimenez J, Lin W, Powers W, Zong X. Prospective motion correction and automatic segmentation of penetrating arteries in phase contrast MRI at 7 T. *Magn Reson Med*. 2022;88:2088-2100. doi: 10.1002/mrm.29364